1	Arm-in-arm response regulator dimers promote intermolecular signal transduction
2	
3	
4	Anna W. Baker, Kenneth A. Satyshur, Neydis Moreno Morales and Katrina T. Forest [#]
5	
6	Department of Bacteriology, University of Wisconsin-Madison, Madison, Wisconsin
7	
8	Running title: Arm-in-Arm Response Regulator Dimers
9	# Address correspondence to Katrina T. Forest, <u>forest@bact.wisc.edu</u>
10	
11	Keywords: bacteriophytochrome, two-component system, response regulator, signal
12	transduction, photoreceptor, arsenic, SAD phasing
13	
14	

Abstract

15

16

17

18

19

20

21

22

23

24

25

26

27

28

29

30

31

32

33

Bacteriophytochrome photosensors (BphPs) and their cognate response regulators make up twocomponent signal transduction systems which direct bacteria to mount phenotypic responses to changes in environmental light quality. Most of these systems utilize single-domain response regulators to transduce signals through unknown pathways and mechanisms. Here we describe the photocycle and autophosphorylation kinetics of RtBphP1, a red light regulated histidine kinase from the desert bacterium Ramlibacter tataouinensis. RtBphP1 undergoes red to far-red photoconversion with rapid thermal reversion to the dark state. RtBphP1 is autophosphorylated in the dark; this activity is inhibited under red light. The RtBphP1 cognate response regulator, RtBRR, and a homolog, AtBRR from Agrobacterium tumefaciens, crystallize unexpectedly as arm-in-arm dimers, reliant on a conserved hydrophobic motif hFWAhL. RtBRR and AtBRR dimerize distinctly from four structurally characterized phytochrome response regulators found in photosynthetic organisms, and from all other receiver domain homodimers in the Protein Data Bank. A unique cacodylate-zinc-histidine tag metal organic framework yielded SAD phases and may be of general interest. Examination of the effect of BRR stoichiometry on signal transduction showed that phosphorylated RtBRR is accumulated more efficiently than the engineered monomeric RtBRR_{mon} in phosphotransfer reactions. Thus, we conclude that arm-inarm dimers are a relevant signaling intermediate in this class of two component regulatory systems.

Importance

BphP histidine kinases and their cognate response regulators comprise widespread red light sensing two-component systems. Much work on BphPs has focused on structural understanding of light sensing, and on enhancing the natural infrared fluorescence of these proteins, rather than on signal transduction or resultant phenotypes. To begin to address this knowledge gap we solved the crystal structures of two single domain response regulators encoded immediately downstream of BphPs. We observed a previously unknown "arm-in-arm" dimer linkage.

Monomerization via deletion of the C-terminal dimerization motif had an inhibitory effect on net response regulator phosphorylation, underlining the importance of these unusual dimers for signal transduction.

Introduction

Bacteria utilize two-component systems (TCS) to monitor and respond to diverse signals in the environment, including the spectrum and intensity of visible light. Light of a specific wavelength may control directed responses, as in the case of phototaxis (1, 2), or can control generalized stress responses (3). Bacteriophytochromes (BphPs) are soluble cytoplasmic red light sensing modules, often histidine kinases (HKs) encoded adjacent to a single domain response regulator (SDRR) to which phosphate is transferred in a light-regulated fashion (4–6). While the mechanism of red light reception by the sensory domains of BphPs is the topic of much active research, and recent work has added to our understanding of the mode of intramolecular signal

transduction by the sensory domains of phytochrome (7–9), the effects of light on phosphate flux through entire pathways are less well-studied. Few phenotypic responses have been conclusively attributed to BphP TCSs, and those that are known suggest the physiological responses controlled by these photoreceptors are as diverse as the environments bacteria inhabit (3, 10–14). Certainly critical to connecting red light sensing to appropriate cellular responses are the bacteriophytochrome RR proteins (BRRs). Thus, we characterized two BRRs structurally and placed them in context of the biochemical activity of a cognate BphP from the Ramlibacter tataouinensis red light sensing TCS. This TCS was revealed by annotation of the genome sequence of this chemotrophic desert microbe, which encodes a high number of putative light sensing proteins (15). Typical BphPs and cyanobacterial phytochromes (Cphs) are dimeric proteins capable of maximal absorbance of red light in the dark state (Pr) which convert to a far-red light absorbing state (Pfr) after exposure to red light. Canonical domain architecture is PerArntSim (PAS) – cGMP phosphodiesterase/adenylate cyclase/FhlA (GAF) – phytochrome specific (PHY) – histidine kinase (HK) (16–18). The PAS domain is the site of covalent chromophore attachment in BphPs, which utilize biliverdin IXa [BV], whereas in Cphs, phycocyanobilin is covalently linked to the GAF domain (18). In all cases, the GAF domain amino acids surround the chromophore. Signal transduction is initiated by a light-driven isomerization of a double bond in this tetrapyrrole (19), and the PHY domain transduces conformational changes to the HK domain. The HK catalyzes ATP hydrolysis and transfers the Y-phosphate to a conserved histidine residue. The transfer is assumed to be to the sister protomer in the dimer, based on sequence comparisons to other trans-

55

56

57

58

59

60

61

62

63

64

65

66

67

68

69

70

71

72

73

74

acting HKs) (20, 21). The kinetics of autophosphorylation of a Cph and subsequent phosphotransfer to its cognate RR have been measured for one example, but have not been reported in detail for non-photosynthetic systems. Psakis, et al. (2011), following an early qualitative report of light regulation of both kinase and phosphotransferase activities (19), reported K_m and k_{cat} values for the Cph1/Rcp1 TCS from Synechocystis sp. PCC 6803 and demonstrated that efficiency of both Cph1 autophosphorylation and phosphotransfer to the RR were four-fold higher in the Pr state (22). Other groups' results support the finding that kinase activity is higher in the Pr state than in the Pfr state for BphPs as well. Giraud, et al. (2005) reported that autophosphorylation by *Rhodopseudomonas palustris* RpBphP2 was 83% reduced in the Pfr state (6). Phosphotransfer to the cognate RR Rpa3017 was also more efficient in the Pr state. Karniol, et al. (2003) reported that Agp1 from Agrobacterium tumefaciens had two-fold greater autophosphorylation activity in the Pr state, and 10-fold greater phosphotransfer to the response regulator AtRR1 (here called AtBRR) in the Pr state (5). The lack of kinetic parameters for BphPs prompted us to characterize the autophosphorylation activities of RtBphP1 as the earliest light regulated step in this TCS signaling cascade. Another hallmark of BV-binding BphPs is their reverse photoconversion from the Pfr state to the Pr state upon exposure to far red light (18). Many are stable in both states, and can be switched to the alternative ground state with the appropriate light stimulus. BphPs can also thermally revert to the Pr state in the absence of light, with a reversion half-life that is characteristic of the particular phytochrome and can be temperature dependent. An example of a poorly stable Pfr form is Agp1, which is relatively unstable at room temperature (23), and displays accelerated

76

77

78

79

80

81

82

83

84

85

86

87

88

89

90

91

92

93

94

95

thermal reversion at 30° C (24). Here we describe reversion kinetics for RtBphP1 and show that RtBphP1 and Agp1 share rapid thermal reversion.

99

100

101

102

103

104

105

106

107

108

109

110

111

112

113

114

115

116

117

Most putative BRRs are annotated as CheY-like SDRRs, which consist of a receiver domain with no obvious regulatory domain such as a DNA-binding motif. For cyanobacterial Cph systems, three such RRs have been characterized by X-ray crystallography: Rcp1 from Synechocystis sp. PCC 6803 (25) (PDB: 113C), RcpA, and RcpB both from Calothrix sp. PCC 7601 (26) (PDB: 1K66, 1K68). This cyanobacterial set has recently been augmented by the structure of Rpa3017 (27). These proteins share a common overall topology with other SDRRs. They consist of an internal parallel five-stranded β-sheet with hydrophobic character surrounded by five α -helices. A conserved aspartate residue protrudes from the terminus of $\beta 3$ and serves as the phosphoacceptor site. Receiver domains can dimerize by one of four known structural arrangements, named for the α-helix and β-strand numbers involved in packing (28). The Rcp-RRs and Rpa3017 all crystallized as unusual inverted 4-5-5 homodimers, and Benda, et al. observed dimers for RcpA and RcpB irrespective of the phosphorylation state (26). The same work noted conservation of consecutive Phe and Trp residues in a C-terminal extension in phytochrome RRs not found in other SDRRs. These residues fold as an α-helix to form a solventexposed hydrophobic patch which interacts with the sister protomer via an aromatic cluster. Here we report the crystal structure of dimeric BRRs from two chemotrophic bacterial species which share the conserved FW key residues, yet form homodimers through a distinct crossover linkage which we propose represents a novel category of RRs. These and arm-in-arm RR dimers may be common to a set of BphP TCSs from non-photosynthetic bacteria.

We investigate the effects of these arm-in-arm dimers on signal transduction, and underline their 118 importance to intermolecular signal transduction in BphP-BRR TCS. 119 120 **Materials and Methods** 121 122 Cloning, expression, and purification of BphPs and BRRs R. tatouinensis strain TTB310 was grown as described (29) and genomic DNA was extracted 123 using a Wizard genomic DNA kit (Promega, Madison, WI). The genes for RtBphP1 and RtBRR 124 were amplified by PCR from R. tataouinensis genomic DNA with primers encoding BamHI and 125 HindIII restriction enzyme sites (RtBphP1 F: 5'-126 127 CGAAGGATCCATGAACCTTCCGCCGCCTGACCTGG-3', RtBphP1 R: 5'-CGAAAAGCTTTTAAGCATGGTTCCTGTCCTCTTTCCTCTTGGGCGGC-3', RtBRR F: 5'-128 129 GGTTGGATCCATGCTTAAACCCATCTTGCTTGTCGAGGACGACAAGC-3', RtBRR R: 130 5'-CCTTAAGCTTTGCTTCGTAGCGGCGCATGGCCTTCATGGACC-3'). These sites were used to clone the genes into plasmid pJ414 encoding an N-terminal hexahistidine tag and tobacco 131 132 etch virus (TEV) protease site (DNA 2.0, Menlo Park, CA) or pET23a encoding a C-terminal hexahistidine tag (EMD Millipore, Billerica, MD), creating pJ414RtBphP1 and 133 pET23aRtBRR_{HIS}, respectively. The gene for RtBRR_{mon} was amplified from pJ414RtBRR using 134 the original forward primer and a reverse primer (R: 5'-135 GGTTAAAAGCTTTTAGCCCAGGTCGGCGATGGCGGCG-3') and then religated into empty 136 pJ414, which resulted in the 5' truncation of 21 codons. The AtBRR gene was codon optimized 137

for expression in E. coli, synthesized and cloned into pJ414, resulting in pJ414AtBRR (DNA 2.0, 138 Menlo Park, CA). 139 Vectors with sequence-confirmed inserts were transformed into BL21(DE3) (AtBRR) or BL21-140 Codon Plus(DE3)-RP (R. tataouinensis genes) (Agilent Technologies, Santa Clara, CA). 141 Overexpression was induced with 1 mM IPTG at OD₆₀₀ of 0.5-0.8 and carried out for 16-18 142 hours at 18° C. Cell pellets from 2 L cultures were resuspended in 30 mL lysis buffer (30 mM 143 Tris pH 8.0, 300 mM NaCl, 10 mM imidazole) and were lysed in a French press. RtBphP1 lysate 144 clarified by centrifugation (30 minutes at 39,190 rcf) was incubated in the dark for 1 hour on ice 145 with 200 µL of 20 mM BV HCl in DMSO (Frontier Scientific, Logan, UT). 146 All chromatography steps were run at 4° C on an Akta Explorer (GE Healthcare, Pittsburgh, 147 PA). RtBphP1, RtBRR_{mon}, and AtBRR were enriched first on a Ni-NTA column (Qiagen, 148 Hilden, Germany) followed by buffer exchange on a 50,000 MWCO or 10,000 MWCO filter 149 (Amicon, EMD Millipore, Billerica, MD) before digestion with TEV protease purified in-house 150 as previously described (30) at 8° C for 16-18 hours. Cleaved species were collected from the 151 flow-through fraction of a second Ni-NTA column and the buffer was changed to 30 mM Tris, 152 pH 8.0 (RtBphP1) or 30 mM tris pH 8.0, 100 mM NaCl, 5% glycerol (BRRs). Proteins were 153 further purified and analyzed for stoichiometry by size exclusion columns Superdex 200 154 (RtBphP1) or Superdex 75 (BRRs) (GE Healthcare, Pittsburgh, PA). The 189 kDa dimer fraction 155 of RtBphP1 was isolated for use in all experiments. Of the proteins in this study, only dimeric 156

RtBRR_{HIS} retained the C-terminal hexahistidine tag, and thus underwent two-step purification with Ni-NTA affinity purification followed by Superdex 75 size exclusion.

BphP spectrophotometry and Pfr half-life determination

157

158

159

160

161

162

163

164

165

166

167

168

169

170

171

172

173

174

175

176

UV-Vis spectra and single-wavelength measurements of RtBphP1 were collected on a Beckman Coulter DU-640B spectrophotometer (Pasadena, CA). All dark state experiments were carried out under dim green light. Spectra were collected on dark-adapted protein which was protected from light for ≥3 hours (dark/Pr state), or illuminated with red light for 1 minute (mixed Pr/Pfr state). Proteins were illuminated with light from a Fostec ACE source filtered with a 700 ± 5 nM bandpass filter (Andover Corp., Salem, NH) which delivered irradiance of 140 umol/m²/s as previously described (31). Illuminated state measurements were limited to spectra recorded no less than 10 seconds after light stimulus removal, by which time thermal reversion was underway. Dark-reversion spectra were recorded on an illuminated RtBphP1 sample for a time course of 10 seconds to 60 minutes after light stimulus removal. Difference spectra were calculated as illuminated absorbance minus Pr absorbance and plotted for each time point. The extinction coefficient (ε_{708}) of RtBphP1 in the Pr state was calculated by solving c_{280} = $A_{280}/\varepsilon_{280}$ using the theoretical ε_{280} . Assuming $c_{280} = c_{708}$, we then measured A_{708} and solved $\varepsilon_{708} = A_{708}/c_{708}$. This yielded ε_{708} of 98.937 M⁻¹ cm⁻¹ for Pr RtBphP1. Notably this simplified method does not take into account contamination by apo-phytochrome, which was estimated at 22% using the extinction coefficient for BV (39,900 M⁻¹ cm⁻¹) at 388 nm (32). Pfr half-lives were determined by measuring A₇₀₈ for the Pr state on a dark-adapted RtBphP1 sample, followed by 1 minute illumination with 700 nm light, then subsequent A₇₀₈ measurement every 30 seconds for 1 hour at 24° C. Three independent experiments were conducted, and a biexponential curve v = Aexp(bt) + Cexp(dt) was fit to the mean data using SigmaPlot dynamic curve fitting (Systat Software, San Jose, CA). The mean and standard deviation of ln(2)/b and ln(2)/d yielded the reported first and second half-lives of the Pfr state, respectively. RtBRR_{HIS} and AtBRR X-ray crystal structure determination and protein interface analysis Purified RtBRR_{HIS} and AtBRR were concentrated to 6.3 mg/mL and 30.0 mg/mL, respectively, in 3000 MWCO centrifugation filters (EMD Millipore, Darmstadt, Germany), and the buffer was changed to 30 mM tris pH 8.0, 100 mM NaCl, 5% glycerol. Hanging drops (33) were set up with 1 µL BRR and 1 µL reservoir solution. RtBRR_{HIS} crystallized with a reservoir solution of 200 mM zinc chloride, 100 mM sodium cacodylate pH 6.5, 10 mM magnesium chloride, and 10% isopropanol. AtBRR crystallized with a reservoir solution of 100 mM tris ph 8.5, 200 mM magnesium chloride, 20% PEG 8000. Three-dimensional, birefringent crystals grew at 19° C within one week (multiple diamond-shaped crystals for RtBRR_{HIS}, single large rods for AtBRR). For data collection, crystals were cryoprotected in mother liquor with 15% glycerol for one minute before vitrification in liquid nitrogen. Diffraction data were collected at the Advanced Photon Source (Argonne National Laboratory, Argonne, IL) on LS-CAT 21-ID-D on a Rayonix MX300 detector (RtBRR_{HIS}) and on LS-CAT 21-ID-F on a Rayonix MX-225 detector (AtBRR). The data were integrated and scaled with HKL2000 (34). For RtBRR_{HIS}, Phaser-MR (35) was used for initial phasing by molecular

177

178

179

180

181

182

183

184

185

186

187

188

189

190

191

192

193

194

195

replacement with search model PDB 1I3C. The structure revealed an interesting dimethylarsenate/zinc interaction with an ordered C-terminal His tag. Even though we collected data at the peak wavelength for Se (0.97910 Å, LS-CAT 21-ID-D) and not As (1.0417 Å) or Zn (1.2837 Å), we were able to use the anomalous signal and the protein sequence in AutoSolve (36) to independently phase the reported structure. The measurability of the anomalous signal was 0.0619 at 2.58 Å resolution (37) with peaks found for one As and three Zn²⁺ ions. The experimentally-phased electron density map revealed all but the N-terminal 6 of the 166 amino acids in the protein. The cacodylate sits on a two-fold rotation axis and was refined at half occupancy. For AtBRR, Phaser-MR was used for phasing by molecular replacement using RtBRR_{HIS} as the search model. Model fitting was done in Coot (38) and refinement was done using Phenix.refine (37). Coordinate and structure factor files were deposited in the Protein Data Bank under codes 5BRI and 5BRJ, for RtBRR_{HIS} and AtBRR, respectively. Coordinate files for AtBRR and RtBRR_{HIS} were submitted to the Proteins, Interfaces, Surfaces, and Assemblies (PISA) web server (39) to predict biologically relevant dimer interfaces from the crystal structures; the same analysis was performed on BRR structures from cyanobacteria: Rcp1 (25), RcpA and RcpB (26). Grand average of hydropathicity (GRAVY) scores were computed for the hFWAhL motif from AtBRR, RtBRR, Rcp1, RcpA, RcpB, Deinococcus radiodurans A0049, and R. palustris Rpa3017 using ExPasy ProtParam (40). Surface electrostatics for RtBRR (without cloning tag residues) were generated using the APBS server (41, 42) and visualized in PyMol.

Autophosphorylation kinetics and phosphotransfer profiling

197

198

199

200

201

202

203

204

205

206

207

208

209

210

211

212

213

214

215

216

218	Autophosphorylation reactions were carried out at room temperature under green safe lights or
219	over a 700 nm LED panel (230 μ mol/m²/s). Reactions contained 5 μ M RtBphP1 in kinase buffer
220	(150 mM MES pH 7.5, 150 mM KCl, 5% glycerol, 5 mM MnCl ₂ , 5 mM MgCl ₂ , 2.5 mM DTT)
221	were started with the addition of ATP (6.25-1000 μM cold ATP with 0.03-0.15% $\Upsilon \text{-}^{32}P$ ATP
222	[6000 Ci/mmol, 150 mCi/mL]), and were stopped after 10 seconds with an equal volume of 2X
223	SDS loading buffer (100 mM Tris-HCl pH 6.8, 4% w/v sodium dodecyl sulfate, 0.2%
224	bromophenol blue, 20% v/v glycerol, 200 mM DTT). Samples were not heated or vortexed prior
225	to 15% SDS-PAGE to minimize loss of phosphorylated species. After Coomassie staining,
226	RtBphP1 band slices were cut and added to 4 mL of Bio-safe II scintillation fluid (Research
227	Products International, Mt. Prospect, IL) before recording counts per minute with a Packard Tri-
228	Carb 2100TR Liquid Scintillation Analyzer (Perkin-Elmer, Waltham, MA). Initial rates (mmol
229	32 P~RtBphP1 /sec) were plotted vs. [ATP] to derive V_{max} , K_m , and k_{cat} values (22). The mean and
230	standard deviation from five independent experiments are reported. Previous experiments carried
231	out at constant [ATP] and varying [RtBphP1] were used to ensure this assay was done in the
232	linear range of activity.
233	Radioactive phosphotransfer reactions were carried out at room temperature under green safe
234	lights. Reactions contained 5 μM RtBphP1 plus 15 μM of RR in kinase buffer. First, the
235	autophosphorylation reaction was run for 30 seconds by addition of ATP (1000 $\mu M,0.05\%$ Y-
236	³² P ATP) to RtBphP1, then phosphotransfer was initiated by adding the RR for an additional 30
237	seconds. Reactions were stopped with an equal volume of 2X SDS loading buffer. Samples were
238	run on 20% SDS-PAGE gels, stained prior to exposure to phosphor screen (2-16 hours exposure

time), and imaged on a GE Typhoon FLA-9000. Phosphor band intensities were quantified with ImageJ software (43), including background estimation and normalization for BphP protein amount based on Coomassie staining. Values reported are the mean and standard deviation of three independent experiments. A one-way ANOVA test determined there was a statistically significant difference between groups. A Tukey's honestly significant difference test determined the statistical difference between individual groups.

Phosphotransfer reactions for Phos-tag acrylamide gels contained 5 µM RtBphP1 plus 15 µM of RR in kinase buffer with or without 1 mM ATP and were incubated for 0, 10, 30, and 60 minutes before the addition of 3X SDS loading buffer to stop the reaction. Potentially phosphorylated proteins were placed on ice after the reactions were stopped and separated on 12% SDS-PAGE gels with 100 µM Phos-tag acrylamide (Wako Pure Chemicals, Osaka, Japan) within one hour. Gels were run at 4° C until the dye front ran off, and then stained overnight with SYPRO Ruby before imaging on a GE Typhoon FLA-9000. Band intensities (I) minus background intensity were quantified using ImageJ software. Percent of RR phosphorylated was calculated as

Results

Photoproperties of RtBphP1

 $I_{upper}*100 / I_{upper} + I_{lower}$ for each lane.

In order to begin characterization of the red light-sensing TCS from *R. tataouinensis*, we cloned, expressed, and purified full-length RtBphP1. Size-exclusion chromatography separated RtBphP1 molecules into four distinct size populations corresponding to 771, 300, 189, and 108

kDa (Fig. 1A). The predominant 189 kDa dimer fraction had a molar proportion of BV to BphP 259 of 0.78 as determined by the relative absorbance and extinction coefficients of RtBphP1 ($\varepsilon =$ 260 98,937 at 708 nm) and free BV ($\varepsilon = 39,900$ at 391 nm). This fraction was used to carry out all 261 dark reversion, autophosphorylation and phosphotransfer experiments. 262 Zinc-binding fluorescence assays (data not shown) demonstrated that RtBphP1 covalently binds 263 the added BV chromophore. UV-Vis spectroscopy verified that RtBphP1 is a functional red 264 light-sensing BphP with a Pr dark ground state ($\lambda_{max} = 708$ nm) (Fig. 1B). Exposure of fully 265 dark-adapted RtBphP1 to 700 nm red light for 1 minute induces a relatively unstable Pfr state 266 $(\lambda_{\text{max}} \sim 750 \text{ nm})$, which thermally reverts to the Pr state (Fig. 1B, 1C) with an unexpected 267 biphasic behavior and half-lives of 0.7 and 20.4 minutes (Fig. 1D). 268

RtBphP1 is a light-regulated autokinase

269

270

271

272

273

274

275

276

277

RtBphP1 acts as a light-regulated autokinase as evidenced by radiolabeled phosphorylation reactions and their associated Michaelis-Menten kinetic constants (Fig. 2). The protein is autophosphorylated in the dark, and this activity is modestly suppressed by 700 nm light. The initial rate of autophosphorylation is slow, and is retarded by two-fold under red light (dark $k_{cat} = 2.0 \pm 0.1 \times 10^{-5} \text{ s}^{-1}$ versus red $k_{cat} = 0.9 \pm 0.3 \times 10^{-5} \text{ s}^{-1}$). Red light acts as a noncompetitive inhibitor of autokinase activity as indicated by unchanged K_m values for ATP (for Pr and Pr/Pfr $K_m = 12.9 \pm 3.5 \,\mu\text{M}$ and $13.6 \pm 6.0 \,\mu\text{M}$, respectively) despite modulated k_{cat} .

AtBRR and RtBRR_{HIS} are novel arm-in-arm dimers

In order to probe intermolecular signal transduction by BphPs, we solved the crystal structure of
RtBRR, the putative cognate RR of RtBphP1, in the non-phosphorylated state. Crystal growth
and phasing were made possible by the inclusion of a C-terminal 14-residue tag ending in
hexahistidine, which is well-ordered and coordinated by zinc and cacodylate ((CH ₃) ₂ AsO ₂ H)
(Fig. 3A). In fact, the zinc and As atoms provided strong anomalous signal, and we were able to
phase the RtBRR $_{\rm HIS}$ structure with a ${\rm Zn}^{2^+}\!/{\rm As}$ single-wavelength anomalous dispersion data set.
This technique should be of general use to solve protein structures that have a histidine tag by
crystallizing the cacodylate/zinc/His complex, since the number of structures in PDB with His
tags is rapidly increasing (44). This strategy is similar to a new general method that has been
proposed for coating the surface of a protein with zinc atoms to solve the phase problem (45).
AtBRR phases were obtained by molecular replacement with RtBRR _{HIS} as the search model
(Fig. 3B). RtBRR $_{HIS}$ was refined to a resolution of 1.9 Å with R_{work}/R_{free} values of 18% and 23%.
AtBRR was refined to a resolution of 1.9 Å with $R_{\text{work}}/R_{\text{free}}$ values of 20% and 24% (Table 1).
As expected, the basic topology of RtBRR _{HIS} is similar to the archetypal SDRR, <i>E. coli</i> CheY
(46) (PDBID: 3CHY, RMSD = 1.3 Å over 70 C_{α} atoms within secondary structure elements).
The common structural features are a hydrophobic five-stranded parallel β sheet core (2-1-3-4-5)
surrounded by five α helices (Fig 4A). The sequence-conserved phosphoaccepting aspartate
(D64 in RtBRR, D65 in AtBRR) is situated at the C-terminal end of $\beta 3$ and faces into the
solvent, accessible for interaction with the cognate BphP HK (Fig. 4A). Both BRR structures had
clear electron density for magnesium ions in the phosphorylation site (Fig. 3B), which are
required for the phosphoryltransfer reaction (47)

The crystal structure of RtBRR_{HIS} revealed an unusual crossover dimer interface geometry that links sister monomers (Fig 4A). The dimer relies on a C-terminal extension with marked structural deviation from known SDRR structures; a bulky hydrophobic \(\beta \) (IFWAVL) that extends from $\alpha 5$, threading through the adjacent monomer before turning back toward the originating protomer via a proline/glycine rich sequence (Fig. 4B). Two antiparallel strands, one from each monomer, form an intermolecular β sheet, evidenced by the presence of six main chain hydrogen bonds. This small sheet is widened by main chain interactions with the loop between α1 and β2 and stapled in place by the side chain of N29, itself invariant among a group of approximately 150 RRs that share the DLGhFWAhLNEPPP sequence (where h is a hydrophobic M/V/L/I residue). Conserved P4 positions the N-terminus for additional interactions at the interface (Fig. 4B). The RtBRR_{HIS} polypeptide ends in a sixth α helix (α 6), which packs against α1 and β2 and is not found in most SDRR structures. Surface electrostatic potential models of RtBRR reveal a sizable cleft between protomers and an extensive positively charged stripe across the dimer surface, either or both of which might serve as an interaction site for signaling partners (Fig. 4C). To ensure that the observed RtBRR_{HIS} dimer interface was not a consequence of stabilizing effects of helix promoting residues or histidine-metal interactions in the cloning tag and to explore BRR stoichiometry in other BphP systems, we also analyzed the interface in the crystal structure of the native sequence AtBRR from A. tumefaciens strain F2. This protein contains all three of the noted N-terminal Pro, α1-β2 loop LxN, and C-terminal DLGhFWAhLNEPPP motifs (Fig. 5). AtBRR dimers were linked by the same bulky hydrophobic β6 (VFWALL) although the

299

300

301

302

303

304

305

306

307

308

309

310

311

312

313

314

315

316

317

318

following proline-rich turn and terminal helix residues could not be modeled due to weak electron density. Given the stabilizing effect of zinc in the crystal structure of RtBRR_{HIS}, size exclusion chromatography runs for RtBRR_{HIS} and AtBRR were performed in metal-free buffer and revealed peaks corresponding to dimers in solution for both species (Fig. 6A, 6B). Analysis of packing interactions of RtBRR_{HIS} and AtBRR using the PISA server (39) confirmed the dominant nature of this hydrophobic crossover strand in stabilizing the dimer. The interface has solvent-inaccessible areas of 1310 Å² ($\Delta G = -20.7$ kcal/mol) and 1400 Å² ($\Delta G = -17.9$ kcal/mol) per monomer for RtBRR (regardless of inclusion of tag residues) and AtBRR, respectively, with both hydrophobic packing and hydrogen bonding playing important roles in the interaction (Table 2).

BRR dimers promote signal transduction

In order to investigate the relevance of the unique arm-in-arm BRR dimers formed by the crossover strand in phosphorelay from BphPs to BRRs, we engineered a monomeric BRR missing the C-terminal 21 amino acids of the native RtBRR sequence. These amino acids correspond approximately to an extension in the sequence compared to canonical SDRRs (Fig.5). Size exclusion chromatography verified that RtBRR_{mon} has a MW in solution of 16 kDa, versus 36 kDa for the RtBRR_{HIS} dimer (Fig. 6A, 6C).

Dark-adapted RtBphP1 dimers were allowed to autophosphorylate at room temperature before the addition of RtBRR_{HIS}, RtBRR_{mon}, or AtBRR, and the transfer of radiolabeled phosphate was visualized by autoradiography. Phosphotransfer was evident to both RtBRR_{HIS} dimer and

RtBRR_{mon} monomer (Fig. 7A), indicating that specificity between the two components was not 340 negatively impacted by the monomer deletion. Specificity for the cognate RR was evident, as 341 RtBphP1 did not transfer phosphate to AtBRR at appreciable levels (Fig. 7A). 342 To assess the relative efficiency of phosphotransfer from RtBphP1 to each BRR, we 343 independently measured both loss of phosphorylated HK (HK*) (Fig. 7A, B) and accumulation 344 of phosphorylated BRR (BRR*) (Fig. 7C, D). In the presence of RtBRR_{HIS} dimer, RtBphP1 was 345 more efficiently dephosphorylated than the HK only phosphorolysis control, with 65% of HK 346 remaining after 30 seconds (Fig 7A, B). However in the presence of RtBRR_{mon} the amount of 347 remaining HK* was actually higher than the basal level (130%). This results may suggest that 348 monomeric RtBRR inhibits phosphotransfer from HK* (Fig 8, reaction 2), although other steps 349 in the TCS may be affected (Fig 8). RtBphP1 phosphorylation in the presence of AtBRR was 350 equivalent to the buffer only control, demonstrating phosphotransfer specificity between the 351 352 RtBphP1 and its cognate BRR. 353 In order to examine signal transduction via accumulation of BRR*, RtBphP1 dimers were incubated with RtBRR_{HIS} or RtBRR_{mon} and an excess of ATP before analyzing the level of RR 354 phosphorylation using Phos-tag acrylamide gels (48–50). Phosphotransfer was evident to both 355 RtBRR_{HIS} dimer and RtBRR_{mon} monomer (Fig. 7C), providing confirmation that specificity 356 between the two components was not impacted by the monomerization. Analysis of relative 357 phosphorylation levels of BRRs indicated that RtBRR_{HIS} more rapidly accumulated greater 358 levels of phosphate than RtBRR_{mon} for all time points tested (Fig. 7D). At the final 60 minute 359 time point, RtBRR_{HIS} was 38% phosphorylated compared to 24% RtBRR_{mon} phosphorylated. 360

Thus, monomerization of RtBRR most likely inhibits phosphotransfer from HK* (Fig 8, reaction 2). This experiment does not rule out but downweights the possible major affects of monomerization of RtBRR is on other steps in the TCS including HK autophosphorylation, HK* phosphorolysis and/or intrinsic BRR* dephosphorylation (Fig. 8, reaction 1, 3, 4) because in each case the prediction would be a higher level of RtBRRmon* remaining compared to RtBRR_{HIS}*.

Discussion

Our characterization the *R. tataouinensis* bacteriophytochrome TCS provides autophosphorylation kinetics of a red light repressed HK with rapid thermal dark reversion, reveals structural details of a previously unknown arm-in-arm dimer association for the RR, and demonstrates the importance of the arm-in-arm dimer for efficient signal transduction through the TCS.

The thermal reset of RtBphP1 to the dark, kinetically accelerated signaling state proceeds rapidly (Fig 1D). This behavior, manifested as weak or unstable absorbance at 750 nm in the Pfr state, is also observed in Agp1 from *A. tumefaciens* (23), the cognate BphP for AtBRR. This is contrasted with most other characterized BphPs and Cphs including *D. radiodurans* DrBphP and *Synechocystis* sp. PCC 6803 Cph1, which achieve stable Pfr absorbance states and more slowly decay back to the Pr state, yet can be photoswitched to the Pr state with far red light. The former class may act as single state light sensing switches, which in the absence of light are rapidly activated. The advantage of the latter class is that such BphPs can act as two-state light sensors

contained in a single enzyme, advantageous in environments where sensing the ratio of two light wavelength ranges confers a survival advantage. Potentially, BphPs with unstable Pfr absorbance require a second signal or binding partner to stabilize the far red state, thereby integrating multiple input signals.

RtBphP1 autophosphorylation measurements support the model that red light acts as a non-competitive inhibitor of the BphP transphosphorylation activity (Fig 2). BphP HK dimers with covalently attached BV in the sensory domain can bind ATP in the kinase domain with similar affinity in the Pr and Pfr states. Autophosphorylation proceeds more rapidly in the dark, thus catalytic steps of ATP hydrolysis and/or transfer of the γ -phosphate to histidine are potentially light-regulated. Conformational changes originating in the sensory domains of BphP must be transduced to regulate trans-phosphorylation. The PHY domain tongue-refolding mechanism (7) demonstrated for DrBphP likely contributes to regulation of HK domain activity by repositioning the HK domains on each protomer relative to one other. Perhaps it is surprising that autokinase activity is reduced only two-fold by red light (*in vitro*) if *R. tataouinensis* utilizes this sensor kinase to regulate a process vital to environmental survival. However, ATP hydrolysis and transfer of phosphate to histidine form but one measurable kinetic step that contributes to overall phosphate flux in the TCS (Fig. 8).

The arm-in-arm dimer interface observed for RtBRR_{HIS} and AtBRR (Fig. 9A, 9B) differs from the interface observed in three Cph cognate RR structures and the *R. palustris* Rpa3107 (Fig 9C, 9D) (PDB: 1I3C, 1K66, 1K68, 4ZYL) (25–27) and is distinct from the three other known RR homodimerization modes (28). Although all six structural examples of BphP-associated RRs

form dimers mediated by conserved Phe/Tyr and Trp amino acids, conservation of these two aromatic residues alone does not result in equivalent quaternary structures. The hydropathicity of surrounding amino acids and their influence on local secondary structure determine the quaternary arrangement for these SDRRs as arm-in-arm (Fig 9 A,B) or inverted 4-5-5 dimers (Fig. 9 C,D). In the cyanobacterial RRs, charged and polar residues surround FW and result in high hydrophilicity, quantified by "grand average of hydropathicity" scores of -0.2-0.1 (40) (Table 2). The dimerization motif residues form α5 near the C-terminus, where Phe and Trp jut out to pack against the sister protomer (Fig 9 C,D). In our newly solved BRR structures, bulky hydrophobic residues surround FW and result in high hydrophobicity (hydropathicity scores of 2.6-2.7) (Table 2); α -helices do not form and instead hydrophobic residues are buried within the folded core, leaving main chain atoms to form a hydrogen-bond dominated β-sheet interface (Fig. 9 A,B). More than 150 bacterial SDRRs in currently searchable databases carry the extended C-terminal hydrophobic crossover motif DLGhFWAhLNEPPP plus a Pro near the Nterminus and the LxN motif between α1 and β2. Notably, all of these predicted arm-in-arm dimer SDRRs are found in non-photosynthetic bacteria, most of which are plant pathogens or commensals such as Pseudomonas syringae and Burkholderia glumae (Fig. 5). Future work to elucidate the biological roles of these signaling pathways is needed. The BRR dimers possess greater solvent-inaccessible surface area and greater negative ΔG of dimerization than the six previous examples (Table 2), which suggests the arm-in-arm dimers require a substantial input of energy to dissociate and may maintain the arm-in-arm arrangement regardless of signaling state. Regulation of monomer-dimer equilibrium in response to

402

403

404

405

406

407

408

409

410

411

412

413

414

415

416

417

418

419

420

421

phosphorylation has been suggested as a possible mechanism of signal transduction for the Cph1-Rcp1 TCS (25). Such a transition cannot be ruled out for RtBphP1 and RtBRR, however the predicted thermodynamics for the dimer interface disfavor such a mechanism. Alternatively, one can consider a model in which phosphorylation promotes conversion between inverted 4-5-5 and arm-in-arm dimers, impacting quaternary structure arrangement. How phosphorylation affects other, potentially signal-transducing, regions of the BRR structure remains an open question. The BRR proteins studied here retain the switch tyrosine essential for chemotaxis signaling in the E. coli CheY system (51), and neither the dimer interface nor the C-terminal 6th helix in RtBRR occlude the position occupied by the FliM α -helix, the binding partner for CheY (52). Further structural studies of variants and/or phosphate-analog bound BRRs are warranted to address these questions. The marked biochemical consequences of disrupting the arm-in-arm dimer interface imply that this oligomeric arrangement is the relevant signal receiver in the TCS in vivo (53). Although we cannot define the precise molecular block, we observe an inhibitory effect on both dephosphorylation of RtBphP1* and accumulation of phosphorylated RtBRR* in the presence of RtBRR_{mon} compared to dimeric RtBRR_{HIS}. What new functionalities could be conferred by the novel arm-in-arm dimer compared to a canonical monomeric SDRR? In both experiments conducted, phosphotransfer proceeded to monomeric as well as dimeric forms of RtBRR, thus HK recognition cannot be carried by the C-terminal dimerization motif. *In vivo*, additional BRR interactions that couple the TCS to an appropriate cellular response may require the novel surface generated by the dimer interface or may take advantage of the larger molecular size of a

423

424

425

426

427

428

429

430

431

432

433

434

435

436

437

438

439

440

441

442

dimer compared to a monomeric SDRR. The BphP TCS from *Rhizobium* NT-26 has been shown to branch, with the BphP1 serving as a phosphodonor to both the cognate arm-in-arm BRR (Fig. 5) and a hybrid HK containing a RR domain (50); one might postulate that such complex networks of protein interactions could capitalize on the multiple binding sites presented by a dimeric BRR. Alternatively, arm-in-arm BRR dimers may provide a cooperative mechanism for signal transduction by doubling the local concentration of phosphoacceptor sites. This mechanism might increase efficiency of a RR that acts as a phosphate sink in a multicomponent TCS to fine tune signaling, as has been proposed for the LovR RR in the blue-light regulated LOVHK pathway (54, 55). Generating a molecular picture of how BRRs couple light sensing by BphPs to phenotypic responses is the next major knowledge gap to be addressed. Identifying signal transduction steps beyond phosphorylation of the SDRR remains one of the most elusive areas of BphP research, which will be aided by biochemical and structural knowledge of the pathway proteins.

Funding Information

This work was supported by the National Science Foundation (Graduate Research Fellowship DGE-1256259 to AWB and MCB1518160 to KTF), the National Institutes of Health (Biotechnology Training Grant 5T32GM008349 to AWB), and the U.S. Department of Education (McNair Scholarship PRJ76LQP217A130069 to NMM). This research used resources of the Advanced Photon Source, a U.S. Department of Energy (DOE) Office of Science User

464	Facility operated for the DOE Office of Science by Argonne National Laboratory under Contract
465	No. DE-AC02-06CH11357. Use of the LS-CAT Sector 21 was supported by the Michigan
466	Economic Development Corporation and the Michigan Technology Tri-Corridor (Grant
467	085P1000817).
468	Acknowledgements
469	The authors thank Kittikhun Wangkonant for data collection assistance, Prof. Thierry Heulin for
470	supplying R. tataouinensis strain TTB310, and Prof. Michael Thomas for the use of equipment
471	and facilities.
472	Author Contributions: AWB and KTF conceived and designed the experiments; AWB, KAS, and
473	NMM executed experiments and acquired the data; AWB, KAS, and KTF analyzed and
474	interpreted the data; AWB and KTF wrote the paper with input from all authors.
475	
476	

477 References

- Wilde A, Fiedler B, Borner T. 2002. The cyanobacterial phytochrome Cph2 inhibits phototaxis towards blue light. Mol Microbiol 44:981–988.
- Ng W-O, Grossman AR, Bhaya D. 2003. Multiple light inputs control phototaxis in Synechocystis sp. strain PCC6803. J Bacteriol 185:1599–1607.
- Kumar S, Kateriya S, Singh VS, Tanwar M, Agarwal S, Singh H, Khurana JP, Amla
 DV, Tripathi AK. 2012. Bacteriophytochrome controls carotenoid-independent response
 to photodynamic stress in a non-photosynthetic rhizobacterium, Azospirillum brasilense
 Sp7. Sci Rep 2:872.
- 486 4. **Bhoo SH**, **Davis SJ**, **Walker J**, **Karniol B**, **Vierstra RD**. 2001. Bacteriophytochromes are photochromic histidine kinases using a biliverdin chromophore. Nature **414**:776–779.
- Karniol B, Vierstra RD. 2003. The pair of bacteriophytochromes from Agrobacterium tumefaciens are histidine kinases with opposing photobiological properties. Proc Natl Acad Sci USA 100:2807–2812.
- Giraud E, Zappa S, Vuillet L, Adriano J-M, Hannibal L, Fardoux J, Berthomieu C,
 Bouyer P, Pignol D, Vermeglio A. 2005. A new type of bacteriophytochrome acts in
 tandem with a classical bacteriophytochrome to control the antennae synthesis in
 Rhodopseudomonas palustris. J Biol Chem 280:32389–32397.
- Takala H, Björling A, Berntsson O, Lehtivuori H, Niebling S, Hoernke M, Kosheleva
 I, Henning R, Menzel A, Ihalainen JA, Westenhoff S. 2014. Signal amplification and
 transduction in phytochrome photosensors. Nature 509:245–248.
- 8. **Burgie ES**, **Wang T**, **Bussell AN**, **Walker JM**, **Li H**, **Vierstra RD**. 2014. Crystallographic and electron microscopic analyses of a bacterial phytochrome reveal local and global rearrangements during photoconversion. J Biol Chem **289**:24573–24587.
- Yang X, Ren Z, Kuk J, Moffat K. 2011. Temperature-scan cryocrystallography reveals
 reaction intermediates in bacteriophytochrome. Nature 479:428–432.
- Evans K, Fordham-Skelton AP, Mistry H, Reynolds CD, Lawless AM, Papiz MZ.
 2005. A bacteriophytochrome regulates the synthesis of LH4 complexes in
 Rhodopseudomonas palustris. Photosynth Res 85:169–180.
- 506 11. **Barkovits K**, **Schubert B**, **Heine S**, **Scheer M**, **Frankenberg-Dinkel N**. 2011. Function of the bacteriophytochrome BphP in the RpoS/Las quorum-sensing network of Pseudomonas aeruginosa. Microbiology **157**:1651–1664.
- Davis SJ, Vener A V, Vierstra RD. 1999. Bacteriophytochromes: phytochrome-like photoreceptors from nonphotosynthetic eubacteria. Science **286**:2517–2520.

- 511 13. Jaubert M, Vuillet L, Hannibal L, Adriano J-M, Fardoux J, Bouyer P, Bonaldi K,
- Fleischman D, Giraud E, Vermeglio A. 2008. Control of Peripheral Light-Harvesting
- Complex Synthesis by a Bacteriophytochrome in the Aerobic Photosynthetic Bacterium
- Bradyrhizobium Strain BTAi1. J Bacteriol **190**:5824–5831.
- 515 14. Wu L, McGrane RS, Beattie GA. 2013. Light regulation of swarming motility in
- Pseudomonas syringae integrates signaling pathways mediated by a bacteriophytochrome
- and a LOV protein. MBio 4:e00334–13.
- 518 15. De Luca G, Barakat M, Ortet P, Fochesato S, Jourlin-Castelli C, Ansaldi M, Py B,
- Fichant G, Coutinho PM, Voulhoux R, Bastien O, Maréchal E, Henrissat B, Quentin
- Y, Noirot P, Filloux A, Méjean V, DuBow MS, Barras F, Barbe V, Weissenbach J,
- Mihalcescu I, Verméglio A, Achouak W, Heulin T. 2011. The Cyst-Dividing Bacterium
- Ramlibacter tataouinensis TTB310 Genome Reveals a Well-Stocked Toolbox for
- Adaptation to a Desert Environment. PLoS One **6**:e23784.
- 16. Nambu JR, Lewis JO, Wharton KA, Crews ST. 1991. The Drosophila single-minded
- gene encodes a helix-loop-helix protein that acts as a master regulator of CNS midline
- development. Cell **67**:1157–1167.
- 527 17. **Aravind L**, **Ponting CP**. 1997. The GAF domain: an evolutionary link between diverse
- 528 phototransducing proteins. Trends Biochem Sci **22**:458–459.
- 529 18. Auldridge ME, Forest KT. 2011. Bacterial phytochromes: more than meets the light.
- 530 Crit Rev Biochem Mol Biol **46**:67–88.
- 19. Yeh KC, Wu SH, Murphy JT, Lagarias JC. 1997. A cyanobacterial phytochrome two-
- component light sensory system. Science **277**:1505–1508.
- 533 20. Casino P, Rubio V, Marina A. 2010. The mechanism of signal transduction by two-
- component systems. Curr Opin Struct Biol **20**:763–771.
- 535 21. Casino P, Miguel-Romero L, Marina A. 2014. Visualizing autophosphorylation in
- histidine kinases. Nat Commun **5**:1–10.
- 537 22. Psakis G, Mailliet J, Lang C, Teufel L, Essen L-O, Hughes J. 2011. Signaling Kinetics
- of Cyanobacterial Phytochrome Cph1, a Light Regulated Histidine Kinase. Biochemistry
- **50**:6178–6188.
- 540 23. Lamparter T, Michael N, Mittmann F, Esteban B. 2002. Phytochrome from
- Agrobacterium tumefaciens has unusual spectral properties and reveals an N-terminal
- chromophore attachment site. Proc Natl Acad Sci U S A **99**:11628–11633.
- 543 24. Njimona I, Lamparter T. 2011. Temperature effects on Agrobacterium phytochrome
- Agp1. PLoS One **6**:e25977.
- 545 25. Im YJ, Rho S-H, Park C-M, Yang S-S, Kang J-G, Lee JY, Song P-S, Eom SH. 2002.
- 546 Crystal structure of a cyanobacterial phytochrome response regulator. Protein Sci 11:614–

- 547 624.
- 548 26. **Benda C**, **Scheufler C**, **De Marsac NT**, **Gartner W**. 2004. Crystal structures of two cyanobacterial response regulators in apo- and phosphorylated form reveal a novel
- dimerization motif of phytochrome-associated response regulators. Biophys J **87**:476–487.
- Yang X, Zeng X, Moffat K, Yang X. 2015. Structure of the response regulator RPA3017
 involved in red-light signaling in Rhodopseudomonas palustris. Acta Crystallogr Sect F,
- 553 Struct Biol Commun **71**:1215–1222.
- 554 28. **Gao R**, **Stock AM**. 2010. Molecular strategies for phosphorylation-mediated regulation of response regulator activity. Curr Opin Microbiol **13**:160–167.
- Heulin T, Barakat M, Christen R, Lesourd M, Sutra L, De Luca G, Achouak W.
- 557 2003. Ramlibacter tataouinensis gen. nov., sp. nov., and Ramlibacter henchirensis sp.
- nov., cyst-producing bacteria isolated from subdesert soil in Tunisia. Int J Syst Evol
- 559 Microbiol **53**:589–594.
- Tropea JE, Cherry S, Waugh DS. 2009. Expression and Purification of Soluble His6-Tagged TEV Protease, p. 297–307. *In* Methods in Molecular Biology: High Throughput Protein Expression and Purification. Springer.
- 563 31. **Auldridge ME**, **Satyshur KA**, **Anstrom DM**, **Forest KT**. 2012. Structure-guided engineering enhances a phytochrome-based infrared fluorescent protein. J Biol Chem **287**:7000–7009.
- Shu X, Royant A, Lin MZ, Aguilera TA, Lev-Ram V, Steinbach PA, Tsien RY. 2009.
 Mammalian expression of infrared fluorescent proteins engineered from a bacterial phytochrome. Science 324:804–7.
- 33. McPherson A. 2009. Introduction to Macromolecular Crystallography, 2nd Ed. John
 Wiley & Sons, Hoboken.
- 571 34. **Otwinowski Z**, **Minor W**. 1997. Processing of X-ray Diffraction Data Collected in Oscillation Mode. Methods Enzym **276**:307–326.
- McCoy AJ, Grosse-Kunstleve RW, Adams PD, Winn MD, Storoni LC, Read RJ.
 2007. Phaser crystallographic software. J Appl Crystallogr 40:658–674.
- 575 36. **Terwilliger TC**, **Adams PD**, **Read RJ**, **McCoy AJ**, **Moriarty NW**, **Grosse-Kunstleve**576 **RW**, **Afonine P V**, **Zwart PH**, **Hung L-W**. 2009. Decision-making in structure solution
 577 using Bayesian estimates of map quality: the PHENIX AutoSol wizard. Acta Crystallogr
 578 Sect D Biol Crystallogr **65**:582–601.
- Adams PD, Afonine P V, Bunkóczi G, Chen VB, Davis IW, Echols N, Headd JJ,
 Hung L-W, Kapral GJ, Grosse-Kunstleve RW, McCoy AJ, Moriarty NW, Oeffner R,
 Read RJ, Richardson DC, Richardson JS, Terwilliger TC, Zwart PH. 2010. PHENIX:
- a comprehensive Python-based system for macromolecular structure solution. Acta

- Crystallogr D Biol Crystallogr **66**:213–221.
- 584 38. **Emsley P, Cowtan K**. 2004. Coot: model-building tools for molecular graphics. Acta Crystallogr D Biol Crystallogr **60**:2126–2132.
- 586 39. **Krissinel E**, **Henrick K**. 2007. Inference of macromolecular assemblies from crystalline state. J Mol Biol **372**:774–797.
- 588 40. Gasteiger E, Hoogland C, Gattiker A, Duvaud S, Wilkins MR, Appel RD, Bairoch A.
 589 2005. Protein Identification and Analysis Tools on the ExPASy Server. Proteomics Protoc
 590 Handb 571–607.
- 591 41. **Dolinsky TJ, Czodrowski P, Li H, Nielsen JE, Jensen JH, Klebe G, Baker NA**. 2007. 592 PDB2PQR: expanding and upgrading automated preparation of biomolecular structures 593 for molecular simulations. Nucleic Acids Res **35**:W522–525.
- 594 42. **Baker NA**, **Sept D**, **Joseph S**, **Holst MJ**, **McCammon JA**. 2001. Electrostatics of nanosystems: application to microtubules and the ribosome. Proc Natl Acad Sci U S A **98**:10037–10041.
- 597 43. **Rasband WS**. ImageJ [Software, Version 1.49]. Natl Institutes Heal Bethesda, MD, USA.
- 598 44. Carson M, Johnson DH, McDonald H, Brouillette C, DeLucas LJ. 2007. His-tag impact on structure. Acta Crystallogr Sect D Biol Crystallogr **63**:295–301.
- 600 45. Cha S-S, An YJ, Jeong C-S, Kim M-K, Lee S-G, Lee K-H, Oh B-H. 2012.

 Experimental phasing using zinc anomalous scattering. Acta Crystallogr Sect D Biol
 Crystallogr 68:1253–1258.
- 603 46. **Volz K**, **Matsumura P**. 1991. Crystal structure of Escherichia coli CheY refined at 1.7-Å resolution. J Biol Chem **266**:15511–15519.
- Stock AM, Martinez-Hackert E, Rasmussen BF, West AH, Stock JB, Ringe D, Petsko
 GA. 1993. Structure of the magnesium-bound form of CheY and mechanism of phosphoryl transfer in bacterial chemotaxis. Biochemistry 32:13375–13380.
- 608 48. **Barbieri CM**, **Stock AM**. 2008. Universally applicable methods for monitoring response regulator aspartate phosphorylation both in vitro and in vivo using Phos-tag-based reagents. Anal Biochem **376**:73–82.
- Kinoshita E, Kinoshita-Kikuta E. 2011. Improved Phos-tag SDS-PAGE under neutral pH conditions for advanced protein phosphorylation profiling. Proteomics 11:319–323.
- Wojnowska M, Yan J, Sivalingam GN, Cryar A, Gor J, Thalassinos K, Djordjevic S.
 2013. Autophosphorylation activity of a soluble hexameric histidine kinase correlates with the shift in protein conformational equilibrium. Chem Biol 20:1411–1420.
- 51. **Zhu X**, **Amsler CD**, **Volz K**, **Matsumura P**. 1996. Tyrosine 106 of CheY plays an important role in chemotaxis signal transduction in Escherichia coli. J Bacteriol

619	52.	Dyer CM, Dahlquist FW. 2006. Switched or not?: the structure of unphosphorylated
620		CheY bound to the N terminus of FliM. J Bacteriol 188 :7354–7363.

618

632

178:4208–4215.

- 53. Laub MT, Biondi EG, Skerker JM. 2007. Phosphotransfer profiling: systematic
 mapping of two-component signal transduction pathways and phosphorelays. Methods
 Enzymol 423:531–548.
- Foreman R, Fiebig A, Crosson S. 2012. The LovK-LovR two-component system is a regulator of the general stress pathway in Caulobacter crescentus. J Bacteriol 194:3038–3049.
- 55. Sycz G, Carrica MC, Tseng T-S, Bogomolni RA, Briggs WR, Goldbaum FA, Paris G.
 2015. LOV Histidine Kinase Modulates the General Stress Response System and Affects the virB Operon Expression in Brucella abortus. PLoS One 10:e0124058.
- 56. Stivala A, Wybrow M, Wirth A, Whisstock JC, Stuckey PJ. 2011. Automatic
 generation of protein structure cartoons with Pro-origami. Bioinformatics 27:3315–3316.

Figure Legends

633

Figure 1. Photoproperties of RtBphP1. A. Gel filtration of RtBphP1. Peaks with both 280 nm and 634 700 nm absorbance correspond to RtBphP1 oligomers. Peak C is the dimer fraction used in all 635 experiments. Numbered circles represent sizing standards: (1) thyroglobulin (669 kDa); (2) 636 ferritin (440 kDa); (3) catalase (232 kDa), and (4) aldolase (158 kDa). B. Visible spectra of 637 RtBphP1 in the fully dark-adapted, Pr state (black line), after 1 minute illumination with 700 nm 638 light (red line) and 5-60 minute interval recovery products (gradient of red to dark grey), C. 639 Difference spectra (illuminated minus dark state absorbance) of the data from A. D. Time course 640 and biexponential modeling of Pfr thermal decay at 24° C. The mean data and derived half-lives 641 from three independent experiments are shown. 642 Figure 2. Red-light regulated autophosphorylation of RtBphP1. Michaelis-Menten plot of five 643 independent experiments. Initial rates of formation (mean \pm S.D.) of ³²P-labeled RtBphP1 vs. 644 ATP concentration are compared for activity in the dark state (black) or in the red illuminated 645 state (grey). 646 Figure 3. Electron density maps and models for RtBRR_{HIS} and AtBRR. A. Ordered hexahistidine 647 tags from two RtBRR_{HIS} molecules (one with C grey, one with C orange, both with O red, N 648 blue) across the crystallographic twofold axis are coordinated by cacodylate (As purple) and zinc 649 ions (slate spheres). Grey mesh: F_o electron density map phased with anomalous signal, 650 contoured at 1 σ . Red mesh: anomalous difference map contoured at 3 σ . B. Detail of the AtBRR 651 phosphoacceptor site including Mg ion (green sphere) coordinated by side chain and main chain 652

atoms and three ordered water molecules (red spheres). The electron density shown is a 2mF₀-653 DF_c simulated annealing composite omit map contoured at 1σ. 654 Figure 4. Structure of arm-in-arm BRR dimers. A. Overview of the RtBRR_{HIS} dimer in which 655 one protomer (grey) links with another (orange, with β6 and α6 highlighted in yellow) to form 656 the arm-in-arm dimer (cloning tag and histidine residues intimated with dashed line). The green 657 sphere represents the Mg ion that marks the phosphoacceptor surface. B: Detail of the RtBRR_{HIS} 658 arm-in-arm dimer interface. B6 from each monomer participates in an intermolecular antiparallel 659 β-sheet; the extensive hydrogen-bonded network also involves N-terminal residues and the loop 660 between a1 and B2. Conserved N29 bridges the quaternary arrangement by hydrogen bonding to 661 main chain atoms of residues 3 and 136. Conserved P4 positions the N-terminus for these 662 interactions. C. Surface interaction potential for the RtBRR dimer. The hFWAhL dimerization 663 motif and D64 are shown as sticks. 664 Figure 5. Multiple sequence alignment of SDRRs encoded near bacteriophytochromes. The F/Y 665 and W conserved in bacteriophytochrome RRs are highlighted (black background, white text). 666 Residues crucial to the arm-in-arm dimer interface observed in RtBRR and AtBRR are also 667 conserved in Pseudomonas syringae (PsBRR), Burkholderia glumae (BgBRR), and Rhizobium 668 NT-26 (RNBRR) RRs (grey background, black text). SDRRs adopting the inverted 4-5-5 dimer 669 interface (Rcp1, RcpA, RcpB, and Rpa3017; α5 residues are shown with grey background, white 670 text) lack most or all of these residues, as does the RR from D. radiodurans (DrAA049). 671

Figure 6. Oligomeric status of BRR proteins determined by gel filtration chromatography (1.4-1.6 mg loaded in each case). Molecular weights are reported for the highest magnitude peak in each panel based on a standard curve. (Non-labeled peaks in panel B are 33.1 kDa and 23.9 kDa). The labeled peaks were isolated and used for downstream experiments. A: RtBRR_{HIS}, B: AtBRR, C:RtBRR_{mon}. Figure 7. Phosphorylation state of TCS partners during phosphotransfer reactions. A. After preincubation with ATP-³²P. RtBphP1 was incubated with listed RR as described in Materials and Methods and visualized by Coomassie stain and phosphoimaging of an SDS-PAGE gel (see Materials and Methods). B. Phosphorylation of RtBphP1 was quantified using the low exposure image in A, normalized to the intensity of Coomassie-stained BphP bands, and plotted as % of basal phosphate remaining. Three independent experiments are plotted as mean \pm S.D.; two asterisks denote p<0.01 in a Tukey's HSD test. C. Phosphorylated RtBphP1 was incubated with RtBRR_{HIS} dimers (first four lanes) or engineered monomers (lanes 5-8) and ATP and imaged on a Phos-tag acrylamide gel (see Materials and Methods). D. SYPRO Ruby stained bands from C were quantified with ImageJ and plotted as % of RR phosphorylated. Figure 8. Simplified schematic for phosphate movement through the RtBphP1 (HK) - RtBRR (RR) TCS, showing four steps that contribute to signal transduction. One or more of these is likely to be impacted by BRR stoichiometry, thus accounting for greater accumulation of phosphate on RtBRR_{HIS} vs. RtBRR_{mon}. (Putative additional members of this TCS are not taken

672

673

674

675

676

677

678

679

680

681

682

683

684

685

686

687

688

689

690

691

into account here.)

Figure 9. Uniqueness of arm-in-arm response regulator dimers and the FW role. A. Topology of
the arm-in-arm dimer seen in RtBRR and AtBRR, characterized by the DLGhFWAhLNEPPP
motif which interacts with N-terminal segment (marked by P4) and $\alpha 1$ - $\beta 2$ connecting loop
(marked by L27, N29). B. Structural view of these motifs in the context of RtBRR. C. Topology
of the inverted 4-5-5 dimer seen in Rcp1, RcpA, RcpB, and Rpa3017, characterized by
hydrophilic residues surrounding the FW key. D. Structural view of the $\beta 5$ - $\alpha 5$ packing
interaction in the context of Rcp1 (PDBID: 1I3C) (25). Topology diagrams were generated using
Pro-origami (56).

Table 1. X-ray data collection and structure determination statistics

Data Collection	RtBRR _{HIS} (5BRI)	AtBRR (5BRJ)
Wavelength, Å	0.9791	0.9787
Resolution*, Å	38.3-1.83 (1.85-1.83)	35.0-1.92 (1.95-1.92)
Space Group	P4 ₁ 22	P4 ₁ 22
Unit Cell (a, b, c (Å))	47.7, 47.7, 193.5	41.0, 41.0, 187.7
Completeness, %	99.8 (98.1)	98.7 (97.0)
#Unique/#measured Reflections	20790/20756	13163/12959
#Anomalous Reflections	37570	-
Redundancy	1.8 (1.8)	27.2 (26.4)
< <u>I</u> / σ I>	22.9 (1.1)	53.2 (23.0)
Wilson B value, Å ²	33.0	23.7
R_{sym}^{\dagger} , %	2.6 (105.)	7.2 (15.5)
Refinement		
Resolution, Å	38.36-1.90 (1.93-1.90)	30.9-1.92 (1.99-1.92)
Reflections/# anomalous	18619/33646	12959
$R_{\text{work}}/R_{\text{free}}, \ddagger \%$	17.5/21.3 (31.5/40.4)	19.6/24.0 (21.7/27.4)
Rms deviations		
Bonds, Å	0.02	0.07
Angles, °	1.64	1.03
Ramachandran statistics, %		
Allowed	98.8	96.3
Generously allowed	1.2	3.7
# atoms		
protein	1375	1107
ligand	9	1
water	123	135
<b factor="">, Å²		
protein	38.4	26.8
ligand	37.3	20.2
water	52.8	36.6
*The high est masslution him is	: 1: - 4 - 1 : 41	

^{*} The highest resolution bin is indicated in parentheses.

 $^{^{\}dagger}$ R_{sym} = $\Sigma \Sigma j | Ij - \langle I \rangle$ | ΣIj , where Ij is the intensity measurement for reflection j and $\langle I \rangle$ is the mean intensity for multiply recorded reflections.

 $^{^{\}ddagger}$ R_{work}/R_{free} = $\Sigma ||F_{obs}|| - |F_{calc}||/|F_{obs}|$, where the working and free R factors are calculated by using the working and free reflection sets, respectively. For the R_{free}, 5-10% of the total reflections were held aside throughout refinement.

Table 2. Statistics for phytochrome cognate RR dimer interfaces (calculated using ProtParam andPISA).

Protein	Crossover	Interface area	ΔG	Hydropathicity	# residues in	# h-bonds in
(PDB ID)	motif	per monomer	(kcal/mol)	score ¹ for	interface (per	interface
		(\mathring{A}^2)		motif	monomer)	
RtBRR (5BRI)	IFWAVL	1309.7	-20.7	2.70	30	16
AtBRR (5BRJ)	VFWALL	1399.9	-17.9	2.58	30	24
Rcp1 (1I3C)	SFWLET	1172.5	-13.3	0.12	29	19
RcpA (1K68)	EFWLSY	1104.9	-15.3	0.02	27	11
RcpB (1K66)	KYWLDI	1248.4	-13.0	-0.22	33	18
Rpa3017 (4ZYL)	HFWMNT	1164.9	-7.5	-0.60	33	16

¹ Grand average of hydropathicity (40).

712

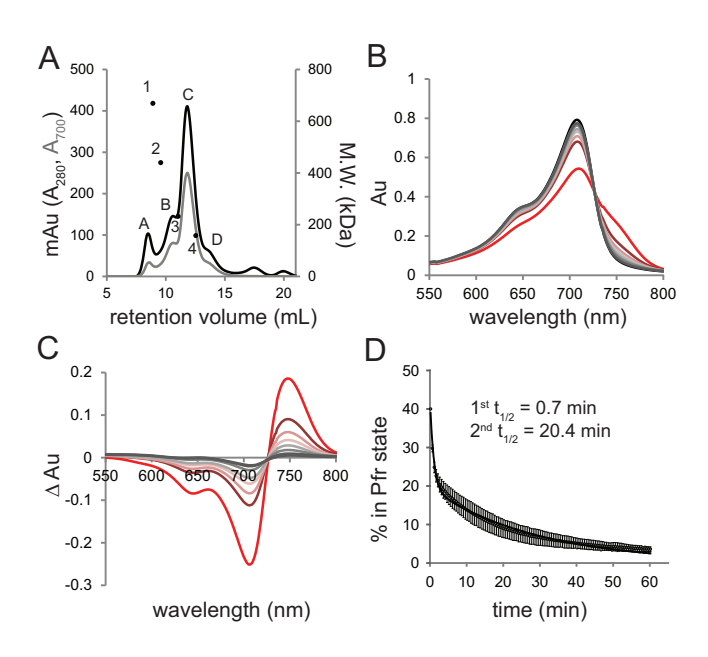


Figure 1. Photoproperties of RtBphP1. A. Gel filtration of RtBphP1. Peaks with both 280 nm and 700 nm absorbance correspond to RtBphP1 oligomers. Peak C is the dimer fraction used in all experiments. Numbered circles represent sizing standards: (1) thyroglobulin (669 kDa); (2) ferritin (440 kDa); (3) catalase (232 kDa), and (4) aldolase (158 kDa). B. Visible spectra of RtBphP1 in the fully dark-adapted, Pr state (black line), after 1 minute illumination with 700 nm light (red line) and 5-60 minute interval recovery products (gradient of red to dark grey). C. Difference spectra (illuminated minus dark state absorbance) of the data from A. D. Time course and biexponential modeling of Pfr thermal decay at 24° C. The mean data and derived half-lives from three independent experiments are shown.

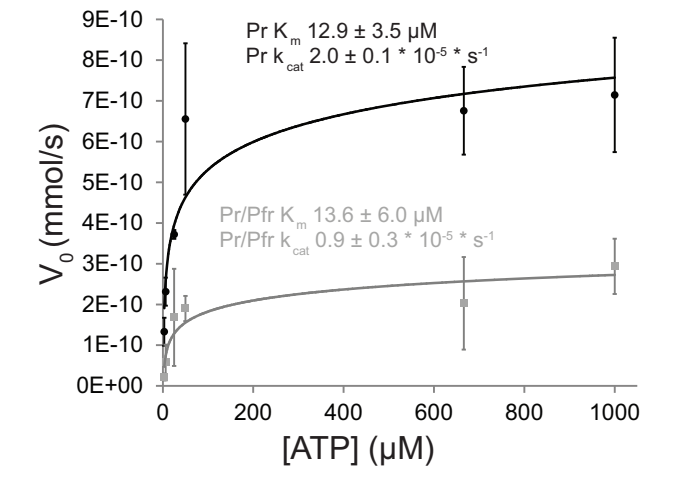


Figure 2. Red-light regulated autophosphorylation of RtBphP1. Michaelis-Menten plot of five independent experiments. Initial rates of formation (mean ± S.D.) of ³²P-labeled RtBphP1 vs. ATP concentration are compared for activity in the dark state (black) or in the red illuminated state (grey).

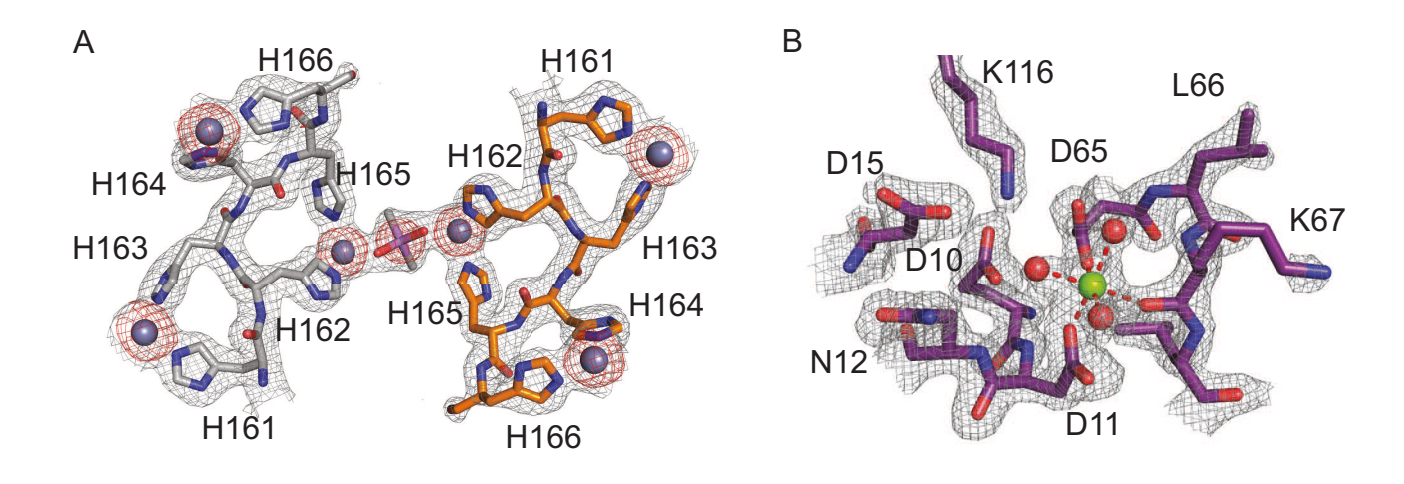


Figure 3. Electron density maps and models for RtBRR $_{HIS}$ and AtBRR. A. Ordered hexahistidine tags from two RtBRR $_{HIS}$ molecules (one with C grey, one with C orange, both with O red, N blue) across the crystallographic twofold axis are coordinated by cacodylate (As purple) and zinc ions (slate spheres). Grey mesh: Fo electron density map phased with anomalous signal, contoured at 1σ . Red mesh: anomalous difference map contoured at 3σ . B. Detail of the AtBRR phosphoacceptor site including Mg ion (green sphere) coordinated by side chain and main chain atoms and three ordered water molecules (red spheres). The electron density shown is a 2mFo-DFc simulated annealing composite omit map contoured at 1σ .

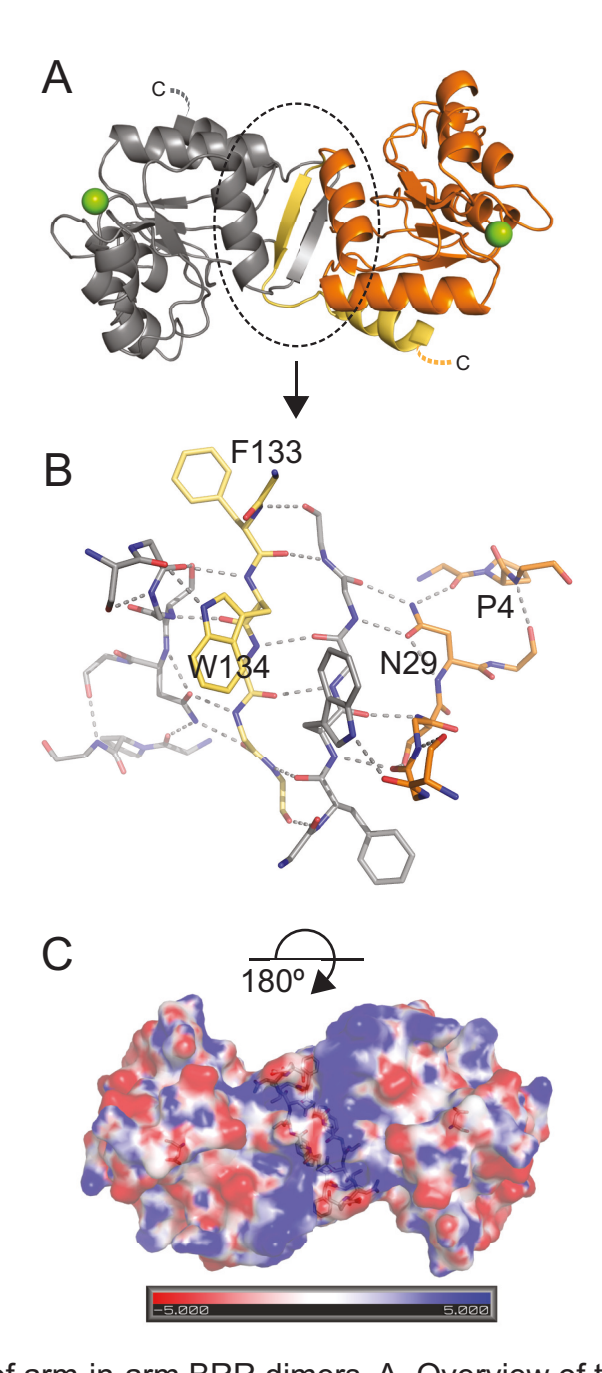


Figure 4. Structure of arm-in-arm BRR dimers. A. Overview of the RtBRR $_{HIS}$ dimer in which one protomer (grey) links with another (orange, with β 6 and α 6 highlighted in yellow) to form the arm-in-arm dimer (cloning tag and histidine residues intimated with dashed line). The green sphere represents the Mg ion that marks the phospho-acceptor surface. B: Detail of the RtBRR $_{HIS}$ arm-in-arm dimer interface. β 6 from each monomer participates in an intermolecular antiparallel β -sheet; the extensive hydrogen-bonded network also involves N-terminal residues and the loop between α 1 and β 2. Conserved N29 bridges the quaternary arrangement by hydrogen bonding to main chain atoms of residues 3 and 136. Conserved P4 positions the N-terminus for these interactions. C. Surface interaction potential for the RtBRR dimer. The hFWAhL dimerization motif and D64 are shown as sticks.

RtBRR	MLK P ILLVEDDKRDLELTLVALERSK L S N EVIVVRDGAQALDYLNREGDFRARE-EGNPAVILLDLKLPKVNGL	73
AtBRR	mpelr $oldsymbol{p}$ illvedn $oldsymbol{p}$ rdle $oldsymbol{L}$ talekc $oldsymbol{Q}$ L $oldsymbol{L}$ Mevvvard $oldsymbol{G}$ Tealdy $oldsymbol{L}$ NVT $oldsymbol{G}$ Syhnr $oldsymbol{p}$ - $oldsymbol{G}$ GDPAVVL $oldsymbol{L}$ DLKL $oldsymbol{K}$ LDLKL $oldsymbol{K}$ VDGL	75
PsBRR	MLK $f P$ ILLVEDNPQDLELTLIALERSQ $f L$ A $f M$ EVIVVRDGAEALDYLFRRDNYAQRL-DGNPAVLLLDLKLPKVDGL	73
BgBRR	MLR $oldsymbol{ t P}$ ILLVEDNPDDIELTMIALEKTR $oldsymbol{ t L}$ A $oldsymbol{ t N}$ PVVSVRDGEEALQFLRREGKWAARP-DESPAVILLDKKLPKLDGH	73
RNBRR	LPELR $f P$ ILLVEDSPRDLELTLAALEKCQ $f L$ A $f N$ EIVIARDGAEAIDYLFGTGTYEGRP-EGDPTVVLLDLKLPKVDGL	75
Rcp1	MSDESNPPKVILLVEDSKADSRLVQEVLKTSTIDHELIILRDGLAAMAFLQQQGEYENSPRPNLILLDLNLPKKDGR	77
RcpA	AHKKIFLVEDNKADIRLIQEALANSTVPHEVVTVRDGMEAMAYLRQEGEYANASRPDLILLDLNLPKKDGR	71
RcpB	AVGNATQPLLVVEDSDEDFSTFQRLLQREGVVNPIYRCITGDQALDFLYQTGSYCNPDIAPRPAVILLDLNLPGTDGR	77
Rp3017	-MNRQRTLPTVLVAEDHDYDKLILTEVFARASISADLRFVSDGEQTLDYIYGRNRFADRGDAPYPAIVLLDLNMPRLDGR	78
DrAA049	MPERASVPLRLLLVEDNAADIFLMEMALEYSSVHTELLVARDGLEALELLEQAKTGGPFPDLILLDLNMPRVDGF	75
EcCheY	MADKELKFLVVDDFSTMRRIV-RNLLKELGFNNVEEAEDGVDALNKLQAGGYGFVISDWNMPNMDGL	66
	.::.:* : : : : :: :: :: :: :: :: :: :: :: ::	
RtBRR	EVLQQVRSSTQLRSIPVVMLTSSQEESDVVKSYELGVNAYVVKPVEFKQFVAAIA DLGI<mark>FW</mark>AVLNEPPP GSMKAMRRYE-	152
AtBRR	EVLQTVKGSDHLRHIPVVMLTSSREEQDLVRSYELGVNAFVVKPVEFNQFFKAIQ DLGV<mark>FW</mark>ALLNEPPP GAHRNGG	151
PsBRR	QVLEAVRQSEELRSIPVVMLTSSREEPDLSRAYQLGVNAYVVKPVEFKEFVSAIS DLGI<mark>fw</mark>avlneppp gsvraqrrpgs	153
BgBRR	EVLKIVRGDERLRHIPVVMLTSSREEKDLLRSYDLGVNAYVVKPVAFDDFMAAIN DLGM<mark>EW</mark>AVLNEPPP YQR	145
RNBRR	EVLERVKRNERLRHIPIVMLTSSREEQDLVKSYELGVNAFVVKPVEFNEFFKAIQ DLGV<mark>EW</mark>ALLNEPPP GSLRNGRA	152
Rcp1	EVLAEIKQNPDLKRIPVVVLTTSHNEDDVIASYELHVNCYLTKSRNLKDLFKMVQGIESEWLETVTLPAAPG	149
RcpA	EVLAEIKSDPTLKRIPVVVLSTSINEDDIFHSYDLHVNCYITKSANLSQLFQIVKGIEE FW LSTATLPS	140
RcpB	EVLQEIKQDEVLKKIPVVIMTTSSNPKDIEICYSYSISSYIVKPL <mark>EIDRLTETVQTFIKYWLD</mark> IVVLPEMG	149
Rp3017	KVVRLLRQDETVRHLVVIALSTSESAKHITEAYSIGFNAYLVKPANIADYVEAIRSLWH EW MNTASLPTTEAYRT	154
DrAA049	ELLQALRADPHLAHLPAIVLTTSNDPSDVKRAYALQANSYLTKPSTLEDFLQLIERLTA YW FGTAAIPQTYQPQ	149
EcCheY	ELLKTIRADGAMSALPVLMVTAEAKKENIIAAAQAGASGYVVKPFTAATLEEKLNKIFEKLGM	129
	: : . : : :::	

Figure 5. Multiple sequence alignment of SDRRs encoded near bacteriophytochromes. The F/Y and W conserved in bacteriophytochrome RRs are highlighted (black background, white text). Residues crucial to the arm-in-arm dimer interface observed in RtBRR and AtBRR are also conserved in *Pseudomonas syringae* (PsBRR), *Burkholderia glumae* (BgBRR), and *Rhizobium* NT-26 (RNBRR) RRs (grey background, black text). SDRRs adopting the inverted 4-5-5 dimer interface (Rcp1, RcpA, RcpB, and Rpa3017; α5 residues are shown with grey background, white text) lack most or all of these residues, as does the RR from *D. radiodurans* (DrAA049).

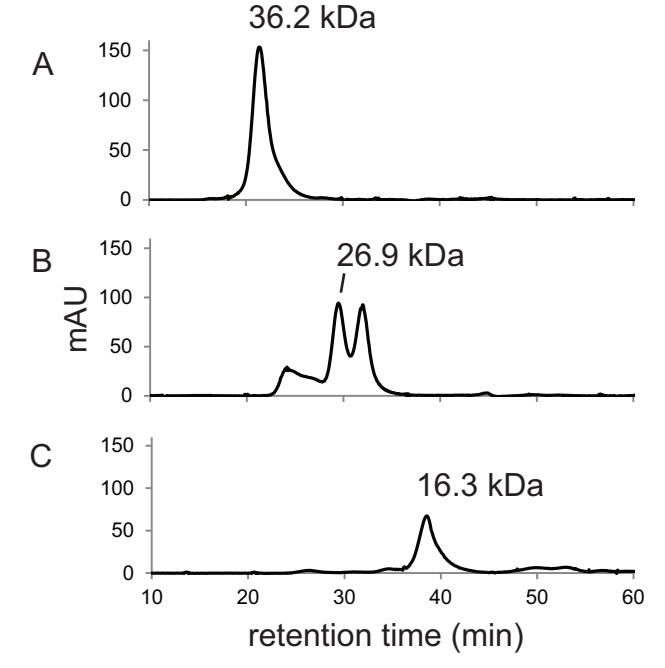


Figure 6. Oligomeric status of BRR proteins determined by gel filtration chromatography (1.4-1.6 mg loaded). Molecular weights are reported for the highest magnitude peak in each panel based on a standard curve. (Non-labeled peaks in panel B are 33.1 kDa and 23.9 kDa). The labeled peaks were isolated and used for downstream experiments. A: RtBRR_{HIS}, B:

AtBRR, C:RtBRR_{mon}.

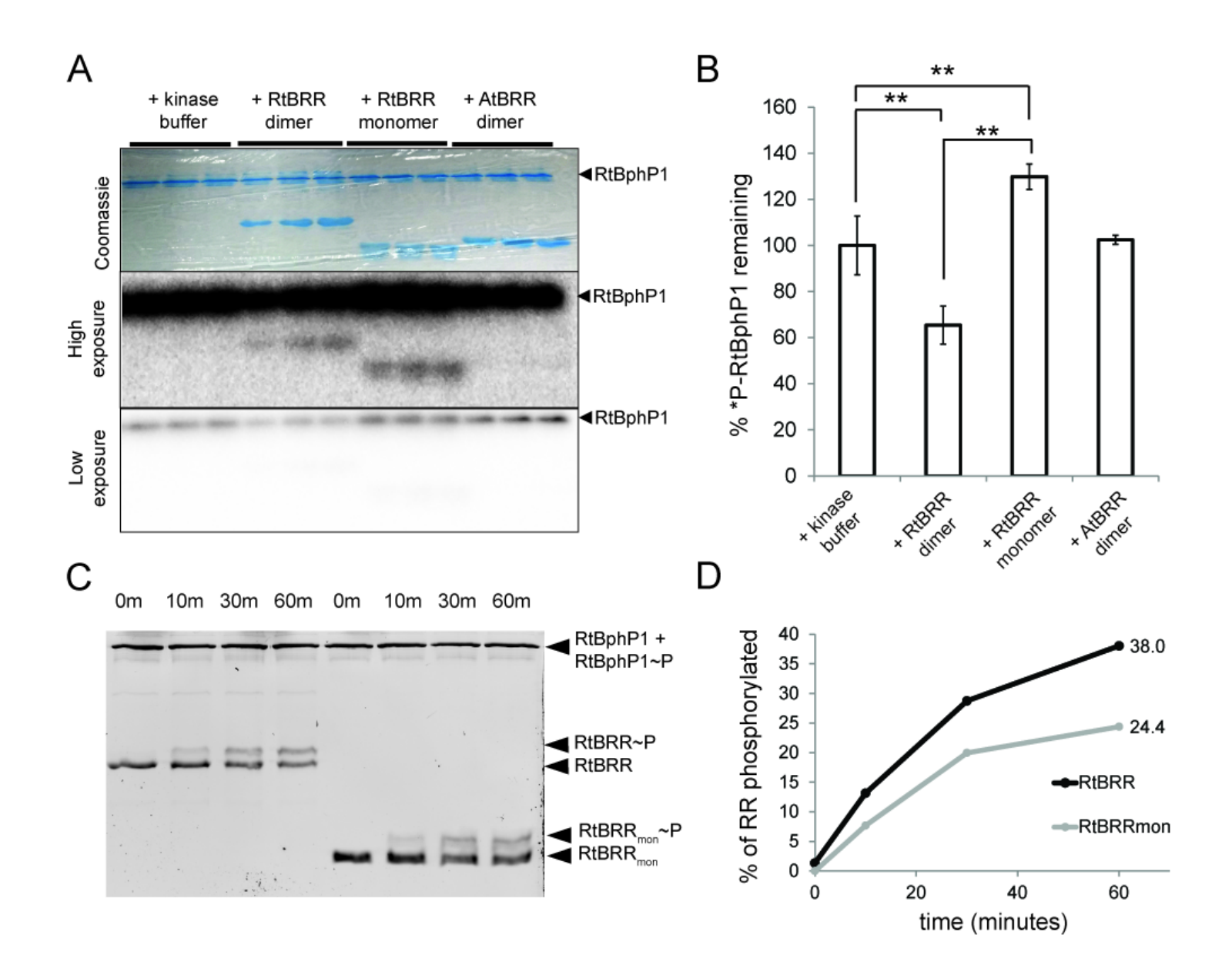


Figure 7. Phosphorylation state of TCS partners during phosphotransfer reactions. A. After preincubation with ATP-32P, RtBphP1 was incubated with listed RR as described in Materials and Methods and visualized by Coomassie stain and phosphoimaging of an SDS-PAGE gel (see Materials and Methods). B. Phosphorylation of RtBphP1 was quantified using the low exposure image in A, normalized to the intensity of Coomassie-stained BphP bands, and plotted as % of basal phosphate remaining. Three independent experiments are plotted as mean ± S.D.; two asterisks denote P < 0.01 in a Tukey's HSD test. C. Phosphorylated RtBphP1 was incubated with RtBRR_{HIS} dimers (first four lanes) or engineered monomers (lanes 5-8) and ATP and imaged on a Phos-tag acrylamide gel (see Materials and Methods). D. SYPRO Ruby stained bands from C were quantified with ImageJ and plotted as % of RR phosphorylated.

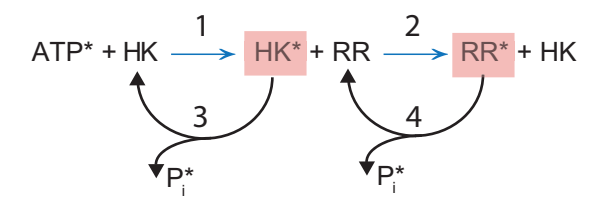


Figure 8. Simplified schematic for phosphate movement through the RtBphP1 (HK) - RtBRR (RR) TCS, showing four overall steps that contribute to signal transduction. Red boxed species are quantified in this paper. One or more of these is likely to be impacted by BRR stoichiometry, thus accounting for greater accumulation of phosphate on RtBRRHIS vs. RtBRRmon. (Putative additional members of this TCS are not taken into account here.)

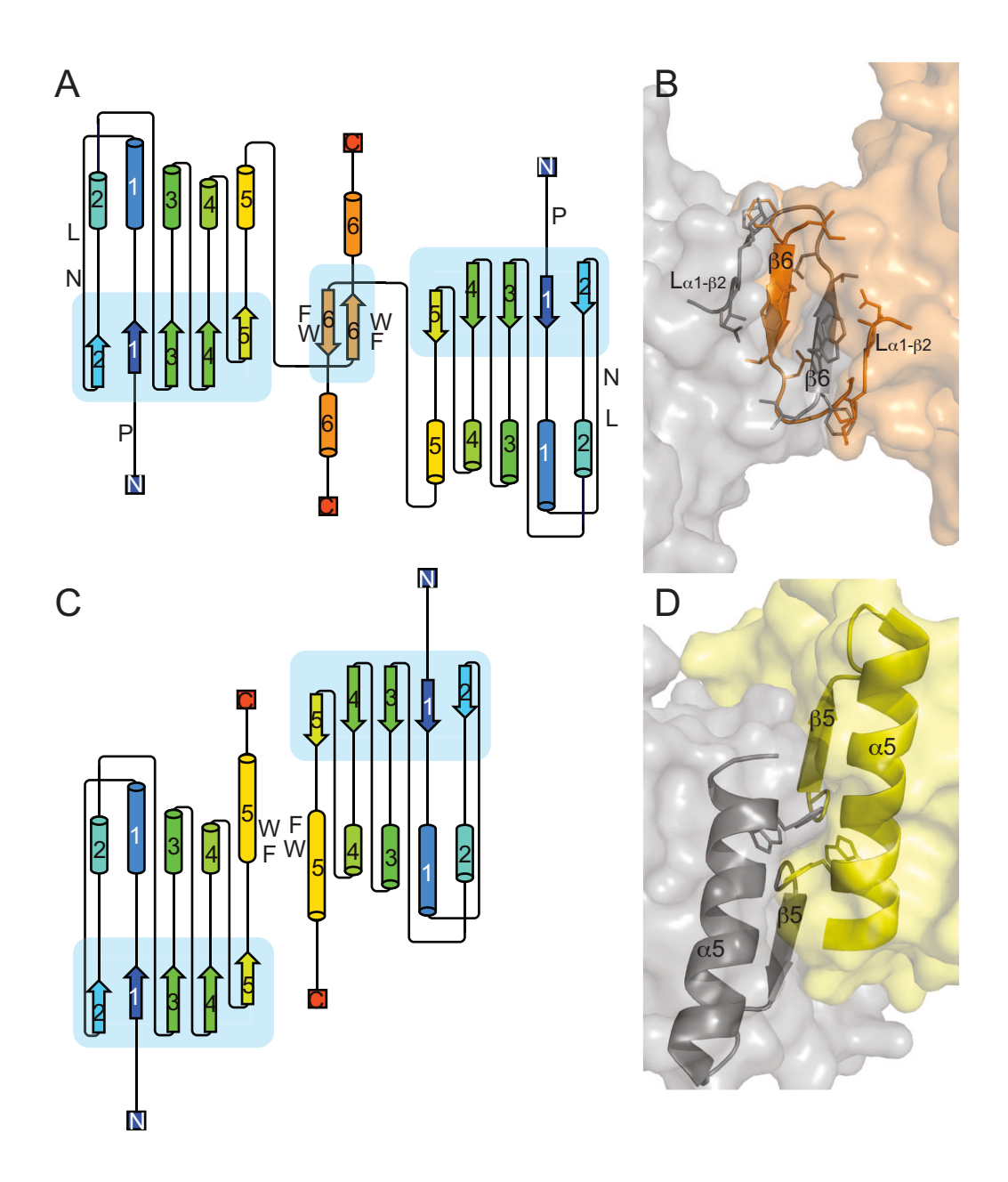


Figure 9. Uniqueness of arm-in-arm response regulator dimers and the FW role. A. Topology of the arm-in-arm dimer seen in RtBRR and AtBRR, characterized by the hGhFWAhLNEPP motif which interacts with N-terminal segment (marked by P4) and α 1- β 2 connecting loop (marked by L27, N29). B. Structural view of these motifs in the context of RtBRR. C. Topology of the inverted 4-5-5 dimer seen in Rcp1, RcpA, RcpB, and Rpa3017, characterized by hydrophilic residues surrounding the FW key. D. Structural view of the β 5- α 5 packing interaction in the context of Rcp1 (PDBID: 113C) (23). Topology diagrams were generated using Pro-origami (54).